Volume 8
Number 11
November 2021
Pages 2861–3164

Materials Horizons

rsc.li/materials-horizons

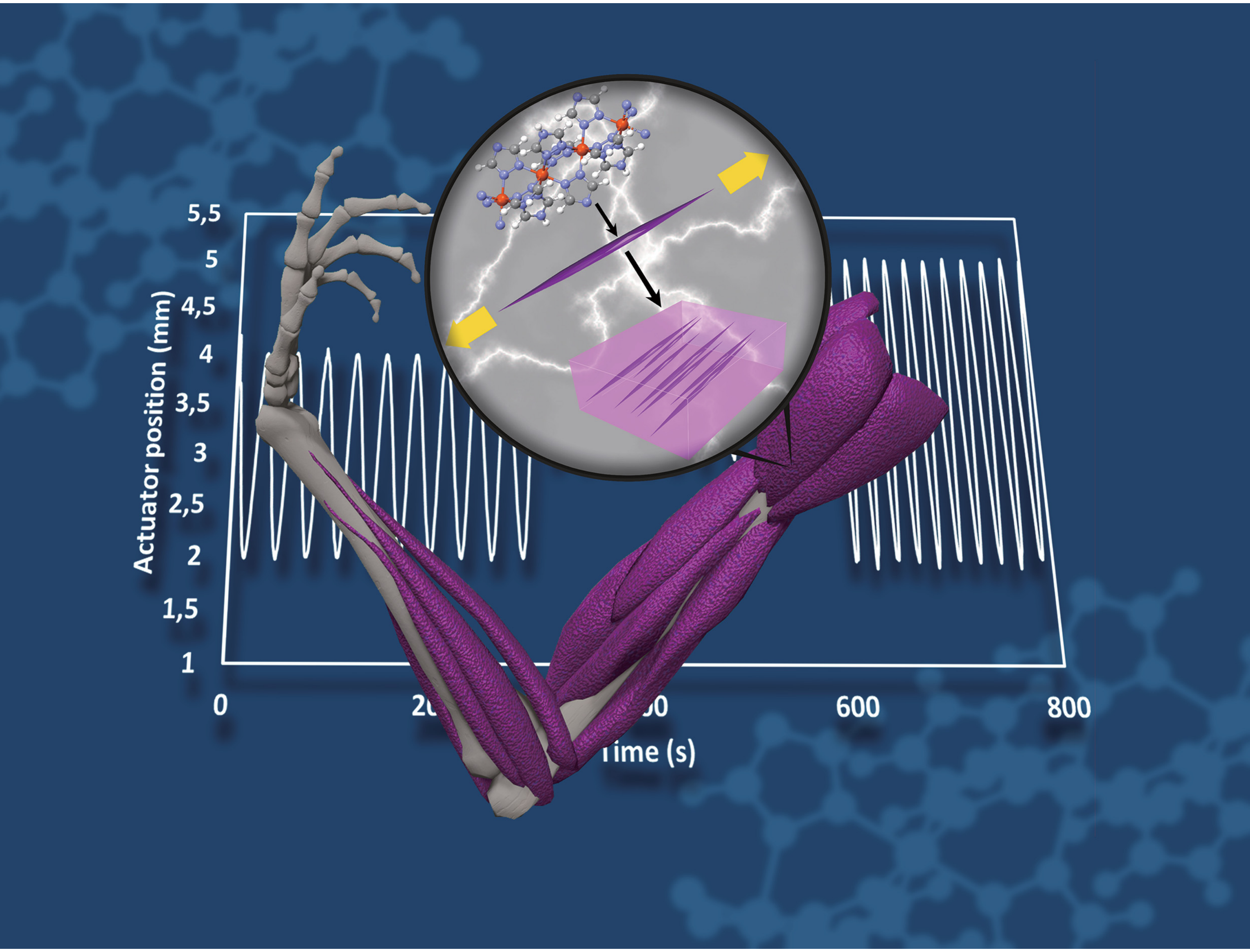

ISSN 2051-6347

ROYAL SOCIETY
OF **CHEMISTRY**

COMMUNICATION
Lionel Salmon, Azzedine Bousseksou *et al.*
Colossal expansion and fast motion in
spin-crossover@polymer actuators

Materials Horizons

ROYAL SOCIETY OF CHEMISTRY

COMMUNICATION

View Article Online
View Journal | View Issue

Check for updates

Cite this: *Mater. Horiz.*, 2021, **8**, 3055

Received 22nd June 2021,
Accepted 3rd September 2021

DOI: 10.1039/d1mh00966d

rsc.li/materials-horizons

Colossal expansion and fast motion in spin-crossover@polymer actuators†

Mario Piedrahita-Bello,[ab] José Elias Angulo-Cervera,[ab]
Alejandro Enriquez-Cabrera,[a] Gábor Molnár,[a] Bertrand Tondu,[b]
Lionel Salmon*[a] and Azzedine Bousseksou*[a]

Bilayer spin crossover (SCO)@polymer nanocomposites show robust and controllable actuation cycles upon an electrical stimulus. The anisotropic shape of the embedded particles as well as the mechanical coupling between the SCO particles and the matrix can substantially intensify the work output of the actuators.

New concepts

Soft, compliant actuators provide genuine prospects for the development of robots and other devices able to interact with delicate objects. Here, we show as a proof of concept that a substantial strain amplification can be derived from tailored elastic interactions between a soft matrix and stiff particles, displaying a transformation strain. To this aim, we synthesized high aspect ratio spin crossover (SCO) particles and aligned them within the matrix to funnel the SCO strain predominantly along the longitudinal direction. This pioneering approach turned out to be powerful and afforded huge transformation strains in dilute composites (25 vol%), which are in excess with respect to the maximum achievable strain in the bulk SCO material. The resulting high work density ($\sim$4 J cm^{-3}) and colossal thermal expansion coefficient ($\sim$4000 ppm K^{-1}) are exploited in electrothermally actuated bilayer devices showing tendril-like folding. We also demonstrate excellent controllability of the actuators by means of a simple PID (proportional-integral-derivative) controller, which allowed for high positioning accuracy (>99%) over extended periods (12 days) and numerous actuation cycles (>35 000). Remarkably, the PID was shown to derive benefit from the non-linear properties of SCO materials to improve the response time by a factor of *ca.* 10.

1. Introduction

Soft robotics is a rapidly growing field of research, which makes use of soft, flexible materials able to twist, bend, deform, move or adapt their shape so as to accomplish specific tasks, with multiple applications in the fields of medicine and manufacturing, such as manipulators interacting with objects, robots traversing unpredictable terrain and devices working in close contact with human beings.[1–5] The development of soft, compliant actuators capable of facing the challenges proposed by soft robotics is crucial for the progress of this field as a whole.[6–8] The most investigated active materials for soft actuators comprise dielectric elastomers, conductive polymers, piezo/ferroelectric materials, stimuli-responsive gels, coiled/twisted polymer fibers and yarns, shape memory materials, fluid-driven materials and photoisomerizable organic polymers.[9–18] Depending on the physical mechanisms underlying the actuation, they can be operated by different stimuli, including electric fields, temperature, pressure, magnetic field, humidity or light irradiation.

Each family of materials comes with flaws and challenges, but the common challenge of the field is the need to combine such radically opposing properties as power and softness or accuracy and adaptability. Composite materials provide an effective approach to circumvent this intrinsic paradox of soft actuators. Indeed, a judicious combination of constituents allows the actuator to be conferred with seemingly opposing properties. A well-studied example is the family of ionic polymer–metal composites (IPMC),[19] which overcome the need for a solvent bath that electroactive hydrogel actuators have. Another example is the integration of carbon nanotubes (and other carbon nanomaterials) into polymer or gel-based actuators to improve their conductivity, strength and actuating properties.[20,21] In other cases, active materials (*e.g.* shape memory alloys and polymers) have been combined with dissimilar materials to confer to the resulting composite a combination of disparate material properties.[22–24]

In this context, we have recently proposed the use of polymer composites of molecular spin crossover (SCO) complexes as actuating materials.[25] Actuation by SCO materials relies on the substantial volume change of the crystal lattice (up to 15%) that accompanies the spin transition between the low spin (LS) and high spin (HS) states of the molecules.[26] Combined with typical elastic moduli of *ca.* 5–15 GPa,[27] this volume change results,

---

[a] *LCC, CNRS & Université de Toulouse (UPS, INP), 31077 Toulouse, France. E-mail: lionel.salmon@lcc-toulouse.fr, azzedine.bousseksou@lcc-toulouse.fr*

[b] *LAAS, CNRS & Université de Toulouse (UPS, INSA), 31400 Toulouse, France*

† Electronic supplementary information (ESI) available: Actuator fabrication and characterization details. See DOI: 10.1039/d1mh00966d

a priori, in high work densities (up to several tens of J cm^{-3}). This outstanding performance, combined with their versatility and multifunctionality, makes SCO compounds very appealing for actuating purposes.[28] Crystalline SCO materials are difficult to machine, but embedding SCO particles into processable polymer matrices readily enables the construction of macroscopic objects of arbitrary three-dimensional geometries, using various advanced manufacturing methods, such as solution casting, electrospinning, spray coating, extrusion, 3D printing, impregnation and sol–gel methods.[29] Besides micro- and macroscale actuator processing,[30,31] the polymer matrix can be used to embed electrical heating elements[32] and sensors,[33] which can afford for a high degree of integration without the need for numerous auxiliary devices.

To transform SCO@polymer composites into functional actuator devices one must, however, efficiently harvest the high work density of the embedded SCO particles at the device level and ensure the controlled deployment of this mechanical work, in terms of position accuracy, reversibility, long-term operation and speed of motion. A first concern here is the dilution of the SCO particles in the polymer matrix. Depending on the details of fabrication, typically 15–30% particle load is permitted, which leads to a proportional loss of the elastic energy density. To compensate for this loss, we decided to synthesize fiber-shaped SCO particles and align them within the matrix to contrive the transformation strain predominantly in the useful direction. This approach turned out to be unexpectedly efficient and afforded for huge transformation strains in dilute composites, which are *in excess* with respect to the maximum achievable strain in the bulk SCO material. We show that this strain amplification arises primarily from the elastic interactions between the stiff particles and the soft matrix, which is maximized in transversely isotropic composites. Despite the inherent non-linearity of the actuator, we also demonstrate excellent controllability of the SCO@polymer actuators by means of a simple PID (proportional–integral–derivative) controller.

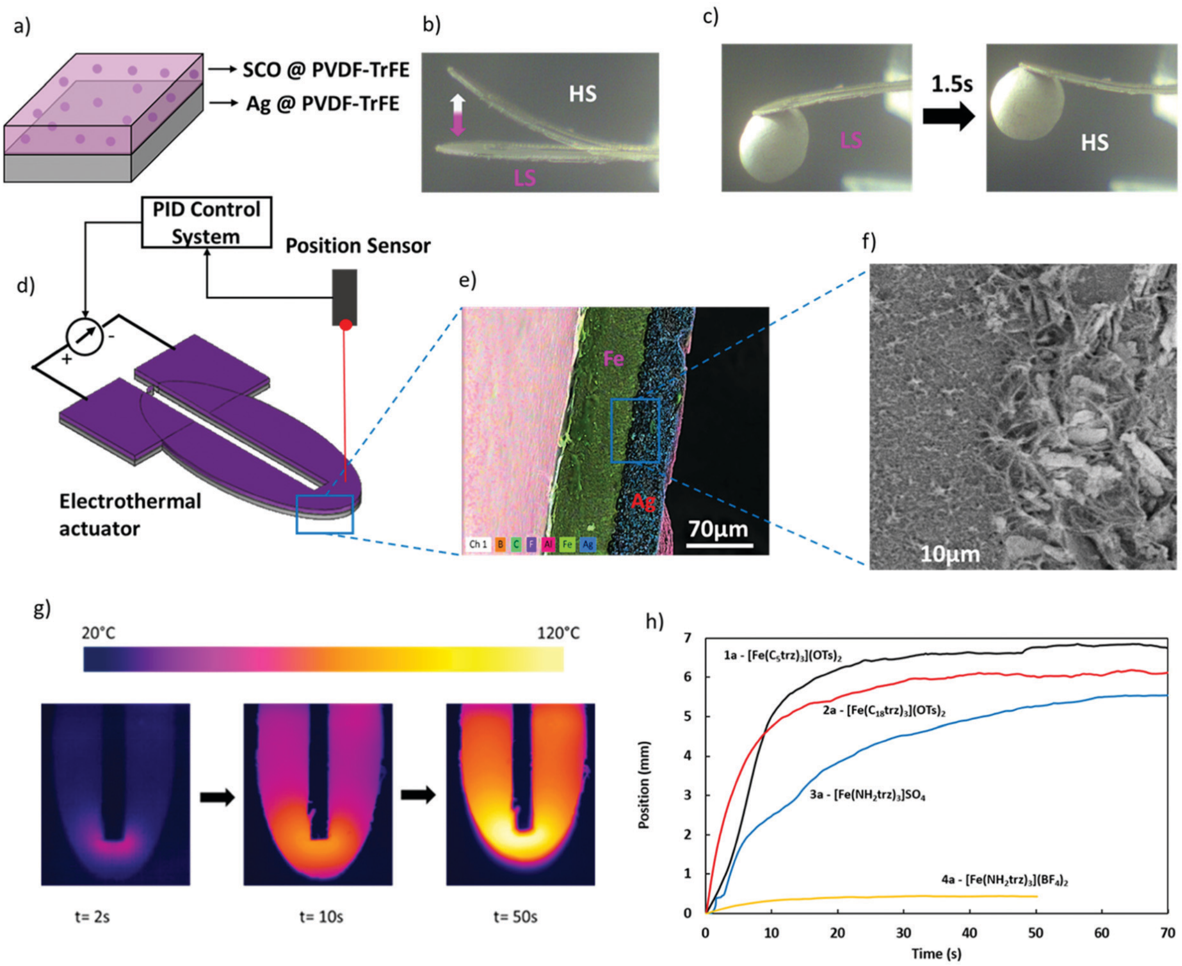

Fig. 1 Structure and principle of operation of the bilayer SCO actuators. (a) Composition of the bilayer system. (b) Reversible actuation of a bilayer device **1a** between the HS and LS states without load and (c) with a load equivalent to 7 times (520 mg) its own weight. (d) Scheme of the actuator test bench indicating the Joule heating, the displacement detection and the PID control. (e) EDX-coupled SEM image of the bilayer cross-section showing the distribution of Fe (green) and Ag (blue) atoms. (f) SEM image of the interface between the two layers. (g) IR thermography images of an actuator on heating. (h) Highest amplitude, open-loop actuation response to a step current input in a series of actuators using different SCO complexes (25 wt%).

Remarkably, the PID can even derive benefit from the non-linear effects, which allow for an improvement of the response time by a factor of *ca.* 10.

2. Actuator design and operation

The proposed electrothermally actuated device is a classical bilayer structure comprised of an active layer with SCO particles (25 wt%) and an electrically conducting layer with silver particles ($\rho \approx 1\ \Omega$ cm), the whole embedded in a monolithic polymer matrix (Fig. 1a) (see the ESI,† for bilayer actuator fabrication and characterization details). The Ag particles allow for efficient Joule-heating, whereas the SCO particles give rise to a large thermal strain at the spin transition. As the matrix, we use poly(vinylidene fluoride-trifluoro-ethylene), P(VDF-TrFE), for its ease of processing,[34] but other polymers like SU8 and PVP could be employed as well.[30,35] The copolymer with 30% TrFE content was chosen for its high Curie temperature – well above the spin transition temperature in the investigated compounds[36] as well as its good mechanical properties and chemical inertness. The macroscopic bilayer films were fabricated by a blade-casting technique and conventional U-shaped devices[37] were cut out using a high precision lathe with a length of 3 cm and a thickness of 150 μm (comprising a 90 μm thick SCO layer and a 60 μm thick conductive layer, see Fig. S12, ESI†). This bilayer device is clamped at one end to a fixture, whereas the other end is left to bend either freely (Fig. 1b) or with payloads (Fig. 1c) under the electro-thermal stimulation (Fig. 1g). The tip position is detected by a non-contact, optical position sensor, which provides the positioning feedback for a standard PID control scheme driving a current source (Fig. 1d). Such bilayers are commonly used actuator structures aimed for amplifying the displacement.[38] However, the large cyclic interfacial stresses result often in delamination – in particular between greatly different materials. The goal of our quasi-monolithic design is to provide strong adhesion for the two dissimilar layers by a common polymer backbone. Energy-dispersive X-ray spectroscopy (EDX) mapping shows well-defined layers (Fig. 1e) that allow the strain mismatch to drive the actuation. Yet, a chemically continuous interface (*i.e.* a polymer fiber network) is evidenced between the two layers in the high-resolution scanning electron microscopy (SEM) images (Fig. 1f), ensuring good mechanical coupling, whilst impeding the delamination of the two strata.

We charged the P(VDF-TrFE) matrix by microcrystalline powders of Fe(II)–triazole SCO complexes. This well-known family of compounds[39] is particularly interesting for actuation purposes due to the large volumetric strains (up to 12%[40]) and the abrupt nature of the spin transition occurring usually above room temperature. The open-loop actuating behavior of selected Fe(II)-triazole SCO complexes is shown in Fig. 1h, which displays the cantilever tip displacement as a function of time in response to the highest current bias, which can be applied to the sample without damaging it. The corresponding deflection amplitudes and bending angles are tabulated for the four investigated actuator samples (**1a**–**4a**) in Table 1. In this study, actuator **4a** is a blank, because the SCO in the compound $[Fe(NH_2trz)_3](BF_4)_2$ occurs well below room temperature. As such, its actuation results exclusively from the thermal expansion mismatch of the two layers. Indeed, this 'blank' device shows an actuation amplitude, which is an order of magnitude smaller than that of actuators **1a**–**3a**, which show spin transition above room temperature. This result proves clearly that the strain associated with the SCO phenomenon plays a crucial role in the movement of the actuators. It is worth to note that actuators **1a**–**3a** show similar behaviors, highlighting the versatility of our approach, which can benefit from the vast library of known SCO complexes. (*N.B.* Differences in the actuator response are linked to the specific spin transition properties of the compounds, such as temperature, abruptness, volume change, anisotropy, and so forth.)

3. Actuator identification and control

A general concern with electrothermally actuated devices, in particular in a clamped beam configuration, is the relatively long response time associated with slow heat transfer.[41] In addition, the combined thermal and mechanical solicitation may alter the material properties on longer time scales, leading to drift and lack of reliability. Closed-loop feedback control *via* a PID controller not only allows for accurate output positioning, but also greatly improves the speed and minimizes the drift of the actuators.[42,43] To investigate the closed-loop performance we show here the results obtained for the actuator device **1a**. (See the ESI† for the control of the other actuators.) We first identified the time-response of the actuator under the form of a simple, overdamped second-order model with two real poles, determined for a set of current steps in the range [0.7 A, 1.2 A] (Fig. 2a). (See the ESI† for more details on the identification.) We have to stress that the applicability of a linear model does not signify the actuator has a linear behaviour. Indeed, a very interesting property emerged from this identification process: while the corresponding damping factor appeared to be approximatively constant, equal to *ca.* 1, the undamped natural

Table 1 Actuator compositions and properties. $T_{1/2}\uparrow$ and $T_{1/2}\downarrow$ stand for the spin transition temperatures on heating and cooling, respectively (C_5trz and C_{18}trz = 4-*n*-alkyl-1,2,4-triazole with *n* = 5 and 18, respectively, NH_2trz = amino-1,2,4-triazole, OTs = tosylate)

Actuator	SCO complex	$T_{1/2}\uparrow$ [K]	$T_{1/2}\downarrow$ [K]	Deflection amplitude [mm]	Bending angle [°]	RT (s)
1a	(1) $[Fe(C_5trz)_3](OTs)_2$	340	315	6.8	20	21
2a	(2) $[Fe(C_{18}trz)_3](OTs)_2$	338	311	6.1	18	30
3a	(3) $[Fe(NH_2trz)_3]SO_4$	345	332	5.5	16	50
4a	(4) $[Fe(NH_2trz)_3](BF_4)_2$	284	279	0.4	1.1	22

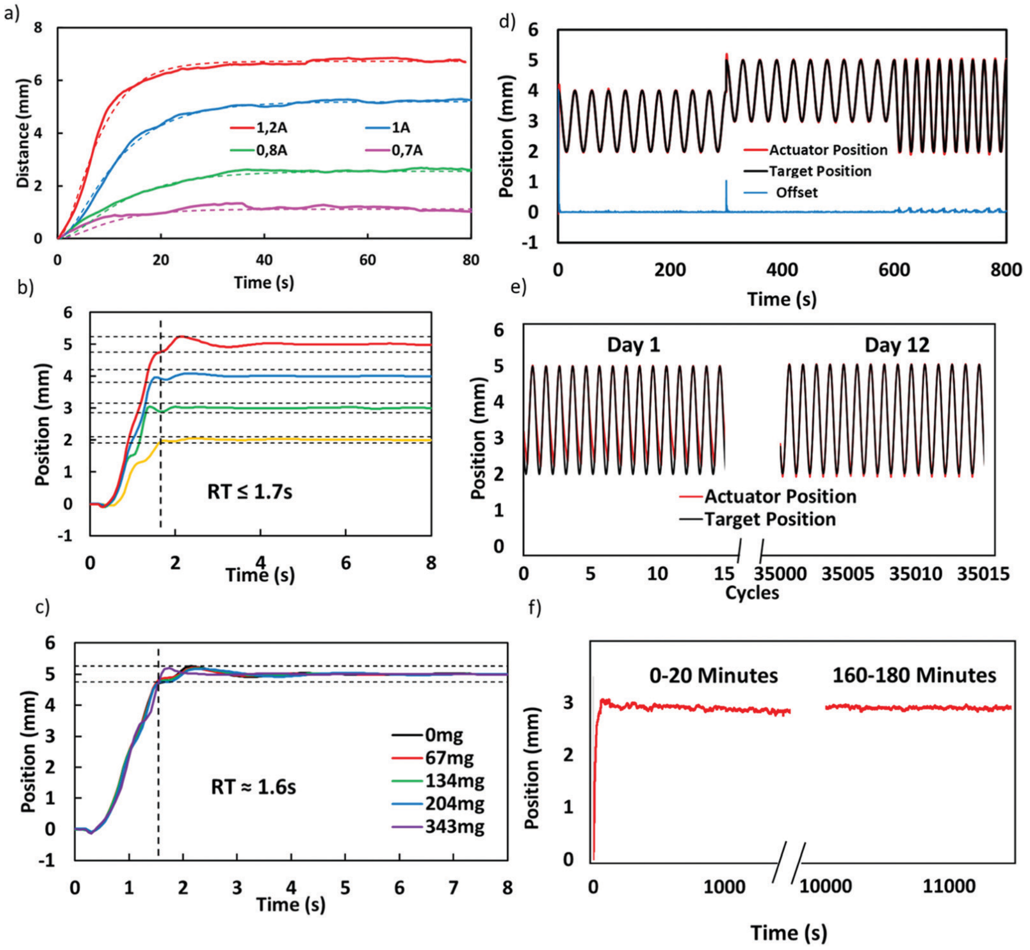

Fig. 2 Actuator control experiments. (a) Open-loop identification of a bilayer device **1a** for different current bias. Dotted lines show the predictions of a second-order linear model. (b) Closed-loop control of the device with target displacements of 5, 4, 3 and 2 mm. The dotted vertical line indicates the response time to 95% of target displacement. Horizontal lines indicate the zone of ±5% error relative to the target displacement. (c) Closed-loop control of the device for a target displacement of 5 mm with different loads. (d) Closed-loop control of the device in response to desired sine-waves with varying control parameters (target displacement, amplitude and frequency). The offset between the target position and the actuator position is also shown. (e) Closed-loop sinusoidal actuation of the device before and after performing 35 000 cycles in ambient air (12 days, 0.033 Hz). (f) Open-loop actuation of the device over a period of 3 hours (I = 0.85 A).

frequency increases monotonously with the current intensity, when the latter becomes superior than *ca.* 0.9 A. This means that, above this threshold current value, the higher the control current value, the faster the response of the system. In steady state, the maximum current is limited to *ca.* 1.2 A. Higher current values are, however, admissible in a closed-loop control, for a few seconds. Using a hand-tuned PID with the possibility of saturating the control current with a value up to 3 A, actuator **1a** was set to move to a series of target positions: 5, 4, 3 and 2 mm (Fig. 2b). This experiment allows us to characterize the response time (RT) of the actuator, which was found in the range of 1–2 s to reach 95% of a given command, which represents an order of magnitude improvement with respect to the open loop RT = 20 s (Fig. 2a). In the case of a linear system, one can expect that a well-tuned PID-control makes possible to reduce the open-loop system response by a factor of 2, which we confirmed by means of a simulation applied to the actuator model assuming a global linear behaviour, whatever the control current value. We interpret thus the 10-fold reduction in time response, resulting from the PID-controller, by the non-linearity of the system: the higher intensity of the admissible current in closed-loop operation leads to a reduced natural frequency and thus faster response (*vs.* the open loop RT). This experiment was repeated with a series of payloads ranging from 1 to 5 times of the weight of the actuator itself (Fig. 2c). The response time was found identical regardless of the load, proving the ability of the actuator to move in a controllable manner under various external loads, which is a key step towards an engineered analogue of natural actuator systems.

To further explore the closed-loop control, the actuator was driven using various sinusoidal waveforms of different amplitudes and frequencies (Fig. 2d). The actuator follows these commands accurately, with an average error of 0.7% of the target position, being even able to follow a change in sinusoidal parameters. To evaluate the long-term stability of the control, the actuator was oscillated with a period of 30 s, at an amplitude of 3 mm, during 12 days for a total of 35 000 actuation cycles. As shown in Fig. 2e, the device showed virtually no sign of fatigue and was able to pursue the command with a standard deviation of *ca.* 0.4 μm for the 35 000 cycles, indicating an important operating life-cycle. It is clear that the natural damping of this kind of bending actuator, put into light during the open-loop identification, plays an important role in closed-loop stability and robustness. It is important to note that, besides the obvious benefits of the close-loop control, the actuator is indeed intrinsically robust. To highlight this resilience, the actuator was subjected to a constant current of 0.85 A during several hours while following its position. After 3 hours the initial position at 2.89 ± 0.04 mm (averaged for the first 20 minutes) has shifted to 2.92 ± 0.02 mm (averaged for the last 20 minutes), denoting no measurable drift within the experimental uncertainty (Fig. 2f). On the same lane, AFM images and variable temperature optical reflectivity measurements performed on bilayer device **1a**, before and after thermal cycling did not show significant variation either (see ESI,† Fig. S16 and S18). We shall remark here that in our study 23 different devices with 17 different compositions and/or concentrations have been fabricated and tested for more than 50.000 actuation cycles altogether and no delamination was observed in any device, which we attribute to a large extent to the monolithic device design.

4. Boosting the actuator performance by material anisotropy

In order to quantify the actuating performance, rectangular bilayers of **1a** were also fabricated and their deflection upon the SCO was assessed under homogenous heating/cooling conditions

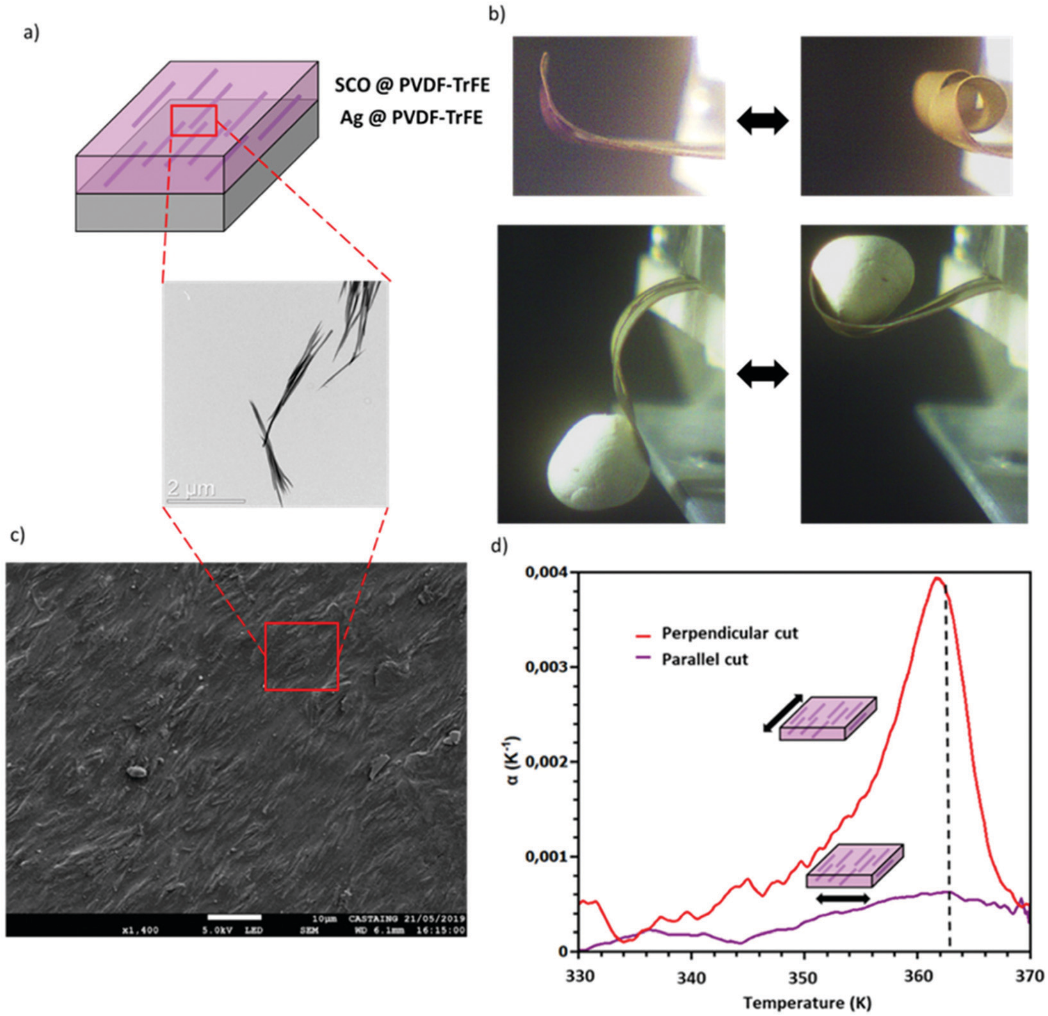

Fig. 3 Preferential particle orientation effect. (a) Scheme of the bilayer device **5a** prepared using rod-like microcrystals of **5** with preferential orientation in the P(VDF-TrFE) matrix. A TEM image of the microcrystals is also shown. (b) Electrothermal actuation of a bilayer device **5a**$_{\parallel}$ with no load (top panel) and with a load equivalent to 9 times (680 mg) its own weight (bottom panel). (c) SEM image of the surface of composite **5a** showing the preferential orientation of the rod-like microcrystals. (d) Linear thermal expansion coefficient of composite **5a** for parallel and perpendicular orientations *vs.* the casting direction. Vertical dotted line indicates the spin transition temperature upon heating.

in a fluid bath. The cantilever curvature change was then analysed using the classical Timoshenko beam theory.[44] From these beam bending experiments (see the ESI† for details), the strain and work density associated with the SCO was evaluated as $\varepsilon_{\mathrm{SCO}} = 1.1\%$ and $W/V_{\mathrm{SCO}} = 0.09\ \mathrm{J\ cm^{-3}}$, respectively. These values are significant with respect to other classes of soft actuators,[9–18] which was showcased by fabricating a gripper device using three bilayers of **1a** (see the ESI†). Yet, it appears necessary, in particular for robotics applications, to further increase the work output of our actuators.

As discussed above, the main driving force behind the actuation of these bilayer systems is the strain that accompanies the SCO phenomenon. As such, the actuator performance can be improved either by increasing the SCO strain or amplifying its impact on the bending motion. We made attempts to increase the strain by simply increasing the concentration of the SCO filler. However, above *ca.* 33 wt% an increase in concentration afforded no further improvement, presumably due to the increasing role of particle–particle interactions. In addition, the mechanical properties of the device started to degrade as well.

More successfully, we have managed to contrive and maximize the SCO strain along the cantilever axis by synthesizing needle-shaped particles and aligning them within the matrix. By virtue of their one-dimensional structure, Fe(II)-triazole chains intrinsically tend to form elongated particles. Notably, the complex $[\mathrm{Fe(Htrz)_2(trz)}](\mathrm{BF_4})$ have been reported to form rod-shaped nanoparticles, whose size and aspect ratio can be conveniently adjusted using a reverse-micelle based synthesis approach.[45] Importantly, it was shown that the rod-shaped particles of this complex display a large volumetric strain (*ca.* 12%) and the direction of the highest linear strain (*ca.* 6.3%) coincides with the long axis of the particles.[40] However, the spin transition in $[\mathrm{Fe(Htrz)_2(trz)}](\mathrm{BF_4})$ overlaps with the Curie transition in the P(VDF-TrFE) matrix, which is an undesirable feature. We have thus undertaken the rational synthesis of $[\mathrm{Fe(Htrz)_{1+y-x}(trz)_{2-y}(NH_2trz)_x(BF_4)_y}]$ solid solutions,[46] wherein the increase of x from 0 to 0.2 afforded a reduction of the SCO temperature to *ca.* 360 K, *i.e.* below the Curie temperature of the matrix. By adjusting the composition of the reverse micelle synthesis medium, we were able to synthesize elongated particles with an aspect ratio of *ca.* 35 (Fig. 3a). These anisometric particles have been then aligned during the actuator fabrication by taking advantage from the fact that the fluid flow during blade casting results in a significant torque.[47] This allowed us to obtain actuator **5a** with highly oriented, needle-like particles of $[\mathrm{Fe(Htrz)_{1.8}(trz)_1(NH_2trz)_{0.2}}](\mathrm{BF_4})_1\cdot 0.7\ \mathrm{H_2O}$ (**5**) (25 wt%) dispersed in the P(VDF-TrFE) matrix, as confirmed by SEM and AFM observations (Fig. 3c, see also the ESI†).

We have then investigated two configurations, **5a**$_{\parallel}$ and **5a**$_{\perp}$, which refer, respectively, to parallel and perpendicular orientations of the bilayers *vs.* the direction of the orientation of the anisotropic particles, which is given by the blade casting direction (see Fig. S2, ESI†). The consequences on the bilayer actuator movement turned out to be impressive: actuator **5a**$_{\parallel}$, rather than bending at an angle as actuators **1a–4a**, folds over itself (Fig. 3b), showing a *ca.* 270 degree spiral winding, reminiscent of nastic movements of tendrils in plants. The device **5a**$_{\parallel}$ can perform this extraordinary movement even while holding a load equivalent to 9 times of its own weight. On the other hand, perpendicular cut bilayer actuators **5a**$_{\perp}$ systematically broke down during the first cycles of actuation, suggesting that particle alignment governs not only the actuation performance, but also the fracture strength of the devices.

Using thermomechanical analysis (see details in the ESI†), we could obtain compelling evidence for the role of the anisotropy of the thermal strain at the origin of the impressive actuating performance of **5a**$_{\parallel}$. Fig. 3c shows the coefficient of thermal expansion (CTE) of the $[\mathrm{Fe(Htrz)_{1.8}(trz)_1(NH_2trz)_{0.2}}](\mathrm{BF_4})_1\cdot 0.7\mathrm{H_2O}$@P(VDF-TrFE) composite measured parallel and perpendicular to the casting direction. For the parallel cut, a colossal CTE of *ca.* 4000 ppm $\mathrm{K^{-1}}$ can be depicted at the spin transition, whereas a *ca.* one order of magnitude inferior CTE occurs in the perpendicular direction. (For comparison, CTE of ordinary materials ranges from 1 to 100 ppm $\mathrm{K^{-1}}$, whereas higher values are coined as 'colossal'.[48])

In the case of actuator **5a**, a quantitative performance analysis directly on the bilayers is not straightforward due to the anisotropy of the system. On the other hand, the thermal expansion measurements actually provide a direct gauge of the strain associated with the SCO, which was determined as 7.1% and 1.7% for **5a**$_{\parallel}$ and **5a**$_{\perp}$, respectively (see the ESI† for measurement details). Astonishingly, the value of 7.1% is much higher than what would be expected for the volume-weighted strain along the particle axis (0.25 × 6.3% = 1.6%) and exceeds even the strain in the oriented, bulk SCO crystal (6.3%). As such, the work density associated with the SCO in **5a**$_{\parallel}$ can be estimated as high as 3.8 J $\mathrm{cm^3}$, which is more than an order of magnitude improvement with respect to actuators **1a** (0.09 J $\mathrm{cm^3}$) and **5a**$_{\perp}$ (0.26 J $\mathrm{cm^3}$). We can rationalize these remarkable findings using micromechanics. Our rationale is based on the theory of coefficient of thermal expansion of composite materials. For generally anisotropic composites constituted of two generally anisotropic phases, Rosen and Hashin[49] has shown that the CTE of the composite is determined by the elastic compliances and CTEs of the constituents and the effective elastic compliance of the composite. Since thermal expansion and SCO strains are equivalent from a mechanical point of view, we can rewrite their result for SCO composites as:

$$\varepsilon_{\mathrm{SCO}_{ij}^{\mathrm{composite}}} = f\varepsilon_{\mathrm{SCO}_{ij}^{\mathrm{particle}}} + \boldsymbol{C}\varepsilon_{\mathrm{SCO}_{kl}^{\mathrm{particle}}} \tag{1}$$

where $\boldsymbol{C}$ is defined by

$$\boldsymbol{C} = P_{klmn}\{S_{mnij}^{\mathrm{composite}} - [fS_{mnij}^{\mathrm{particle}} + (1-f)S_{mnij}^{\mathrm{matrix}}]\} \tag{2}$$

and P_{klmn} is defined by

$$P_{klmn}(S_{mnij}^{\mathrm{particle}} - S_{mnij}^{\mathrm{matrix}}) = I_{klij} \tag{3}$$

with f being the particle volume fraction, S_{ijkl} the elastic compliance tensor and I_{ijkl} the identity tensor. The central idea when writing eqn (1) in this form is to highlight that the effective transformation strain in the composite differs from the volume weighted particle strain (first term) due to the mechanical coupling between the matrix and the particles (second term). As a result, the relationship between $\varepsilon_{\mathrm{SCO}}^{\mathrm{particle}}$ and $\varepsilon_{\mathrm{SCO}}^{\mathrm{composite}}$ is uniquely defined by the elastic compliance of the constituents and that of the composite. As discussed by McMeeking,[50] for dilute composites, the second term in eqn (1) will be negative (resp. positive) if the matrix is stiffer (softer) than the particles. We can thus unambiguously attribute the enhanced transformation strain ($\varepsilon_{\mathrm{SCO}}^{\mathrm{composite}} = 7.1\%$) in composite $\mathbf{5a}_{\parallel}$, with respect to the weighted particle strain ($f\varepsilon_{\mathrm{SCO}}^{\mathrm{particle}} = 1.6\%$), to particle–matrix mechanical interactions. It is important to notice that the alignment of the particles is essential here as it results in the alignment of the shear part of the transformation strain among the particles. Consequently, the effective strain in the transverse isotropic composite **5a** will have both dilatational and the deviatoric components, in contrast to composites with random particle orientation wherein the deviatoric part cancels out.

5. Conclusions

In summary, we demonstrated a facile approach to fabricate and operate bilayer SCO@polymer actuators in a controlled and reproducible manner. These composite materials readily combine the natural compliance and damping of the polymer matrix with the high work density of the spin crossover filler. Owing to their monolithic design, the actuators are robust and resilient. Using a simple PID control, they can maintain accurate positioning capability over more than 35 000 life cycles and can allow for a fast response ($\sim$1 s). Crucially, we find that the mechanical coupling between the SCO particles and the matrix can substantially intensify the work output of the actuators. In particular, we show that the structural anisotropy in transversely isotropic fibrous SCO composites can be used to funnel very efficiently the transformation strain along the cantilever axis leading to a *ca.* 4 J cm^{-3} work output. These findings are not limited to SCO composites and to this specific geometry, but provide a general framework for the design of composite actuators with adjustable properties using advanced micromechanical considerations. The fundamental concept here is that the performance of composite actuators in terms of displacement and force are directly derived from the elastic properties of the constituents and can be purposefully engineered by adjusting the effective elastic compliance of the composite. For a given filler, the choice of the matrix with appropriate elastic properties and the organization of the internal phase geometry are the key parameters for the optimization of the final actuator material.

Author contributions

M. P. B. fabricated and studied the actuators and contributed to the design of experiments, data interpretation and paper writing. A. E. C. synthesized the SCO complexes. J. E. A. C. conducted the thermomechanical analyses. G. M. contributed to the design of experiments, data interpretation and paper writing. L. S. supervised and contributed to all aspects of the project. B. T. carried out the open-loop identification and contributed to the design of experiments, data interpretation and paper writing. A. B. supervised the project. All authors discussed the results and conclusions and commented on the manuscript.

Conflicts of interest

There are no conflicts to declare.

Acknowledgements

We thank financial support from the Federal University of Toulouse/Région Occitanie (PhD grant of MPB), the CONACYT (grants of JEAC and AEC), the Agence Nationale de la Recherche (ANR-19-CE09-0008-01 and the European Commission (H2020-MSCA-RISE-2016, SPINSWITCH, No. 734322)). We are grateful to Gaspard Cereza for his contribution to the construction of the actuator test bench.

References

1 D. Rus and M. Tolley, *Nature*, 2015, **521**, 467–475.

2 G. M. Whitesides, *Angew. Chem., Int. Ed.*, 2018, **57**, 4258–4273.

3 J. D. Madden, *Science*, 2007, **318**, 1094–1097.

4 G. Alici, *MRS Adv.*, 2018, **3**, 1557–1568.

5 S. Kim, C. Laschi and B. Trimmer, *Trends Biotechnol.*, 2013, **31**, 287–294.

6 L. Hines, K. Petersen, G. Z. Lum and M. Sitti, *Adv. Mater.*, 2017, **29**, 1603483.

7 Y. Yang, Y. Wu, C. Li, X. Yang and W. Chen, *Adv. Intell. Syst.*, 2020, **2**, 1900077.

8 N. El-Atab, R. Mishra, F. Al-Modaf, L. Joharji, A. Alsharif, H. Alamoudi, M. Diaz, N. Qaiser and M. Hussain, *Adv. Intell. Syst.*, 2020, **2**, 2000128.

9 C. S. Haines, N. Li, G. M. Spinks, A. E. Aliev, J. Di and R. H. Baughman, *Proc. Natl. Acad. Sci. U. S. A.*, 2016, **113**, 11709–11716.

10 P. Martins, D. M. Correia, V. Correia and S. Lanceros-Mendez, *Phys. Chem. Chem. Phys.*, 2020, **22**, 15163–15182.

11 S. M. Mirvakili and I. W. Hunter, *Adv. Mater.*, 2018, **30**, 1704407.

12 K. Asaka and H. Okuzaki, *Soft Actuators*, Springer, 2014.

13 F. Carpi, R. Kornbluh, P. Sommer-Larsen and G. Alici, *Bioinspir. Biomim.*, 2011, **6**, 045006.

14 K. J. Kim and S. Tadokoro, *Electroactive polymers for robotic applications*, Springer, 2007.

15 L. Ionov, *Langmuir*, 2015, **31**, 5015.

16 T. Mirfakhrai, J. D. W. Madden and R. H. Baughman, *Mater. Today*, 2007, **10**, 30–38.

17 J. D. Madden, N. Vandesteeg, P. A. Anquetil, P. G. Madden, A. Takshi, R. Z. Pytel, S. R. Lafontaine, P. A. Wieringa and I. W. Hunter, *IEEE J. Oceanic Eng.*, 2004, **29**, 706.

18 C. Majidi, *Adv. Mater. Technol.*, 2019, **4**, 1800477.

19 M. Shahinpoor, K. J. Kim and M. Mojarrad, *Artificial muscles*, Taylor & Francis, 2007.

20 J. Foroughi and G. Spinks, *Nanoscale Adv.*, 2019, **1**, 4592–4614.

21 U. Kosidlo, M. Omastová, M. Micusík, G. Ćirić-Marjanović, H. Randriamahazaka, T. Wallmersperger, A. Aabloo, I. Kolaric and T. Bauernhansl, *Smart Mater. Struct.*, 2013, **22**, 104022.

22 W. Wang, Y. Liu and J. Leng, *Coord. Chem. Rev.*, 2016, **38**, 320–321.

23 B. Lester, T. Baxevanis, Y. Chemisky and D. Lagoudas, *Acta Mech.*, 2015, **226**, 3907–3960.

24 A. Miriyev, K. Stack and H. Lipson, *Nat. Commun.*, 2017, **8**, 596.

25 H. Shepherd, I. Gural'skiy, C. Quintero, S. Tricard, L. Salmon, G. Molnár and A. Bousseksou, *Nat. Commun.*, 2013, **4**, 2607.

26 P. Guionneau, *Dalton Trans.*, 2014, **43**, 382–393.

27 M. Mikolasek, M. D. Manrique-Juarez, H. J. Shepherd, K. Ridier, S. Rat, V. Shalabaeva, A. Bas, I. E. Collings, F. Mathieu, J. Cacheux, T. Leichle, L. Nicu, W. Nicolazzi, L. Salmon, G. Molnár and A. Bousseksou, *J. Am. Chem. Soc.*, 2018, **140**, 8970–8979.

28 M. D. Manrique-Juárez, S. Rat, L. Salmon, G. Molnár, C. M. Quintero, L. Nicu, H. J. Shepherd and A. Bousseksou, *Coord. Chem. Rev.*, 2016, **308**, 395–408.

29 A. Enriquez-Cabrera, A. Rapakousiou, M. Piedrahita-Bello, G. Molnár, L. Salmon and A. Bousseksou, *Coord. Chem. Rev.*, 2020, **419**, 213396.

30 M. D. Manrique-Juárez, F. Mathieu, A. Laborde, S. Rat, V. Shalabaeva, P. Demont, O. Thomas, L. Salmon, T. Leichle, L. Nicu, G. Molnár and A. Bousseksou, *Adv. Funct. Mater.*, 2018, **28**, 1801970.

31 M. Piedrahita-Bello, J. E. Angulo-Cervera, R. Courson, G. Molnar, L. Malaquin, C. Thibault, B. Tondu, L. Salmon and A. Bousseksou, *J. Mater. Chem. C*, 2020, **8**, 6001–6005.

32 I. A. Guralskiy, C. M. Quintero, J. Sánchez Costa, P. Demont, G. Molnár, L. Salmon, H. J. Shepherd and A. Bousseksou, *J. Mater. Chem. C*, 2014, **2**, 2949–2955.

33 Y. C. Chen, Y. Meng, Z. P. Ni and M. L. Tong, *J. Mater. Chem. C*, 2015, **3**, 945–949.

34 S. Rat, M. Piedrahita-Bello, L. Salmon, G. Molnár, P. Demont and A. Bousseksou, *Adv. Mater.*, 2018, **30**, 1705275.

35 Y. Chen, J. G. Ma, J. J. Zhang, W. Shi, P. Cheng, D. Z. Liao and S. P. Yan, *Chem. Commun.*, 2010, **46**, 5073–5075.

36 M. Piedrahita-Bello, B. Martin, L. Salmon, G. Molnár, P. Demont and A. Bousseksou, *J. Mater. Chem. C*, 2020, **8**, 6042–6051.

37 M. Amjadi and M. Sitti, *Adv. Sci.*, 2018, 1800239.

38 B. Shapiro and E. Smela, *J. Intell. Mater. Syst. Struct.*, 2007, **18**, 181–186.

39 O. Roubeau, *Chem. – Eur. J.*, 2012, **18**, 15230–15244.

40 A. Grosjean, P. Négrier, P. Bordet, C. Etrillard, D. Mondieig, S. Pechev, E. Lebraud, J. F. Létard and P. Guionneau, *Eur. J. Inorg. Chem.*, 2013, 796–802.

41 S. H. Song, J. Y. Lee, H. Rodrigue, I. S. Choi, Y. J. Kang and S. H. Ahn, *Sci. Rep.*, 2016, **6**, 21118.

42 E. Paster, B. P. Ruddy, P. V. Pillai and I. W. Hunter, *ICRA*, 2010, 506–511.

43 Q. Yao, G. Alici and G. M. Spinks, *Sens. Actuators, A*, 2008, **144**, 176–184.

44 S. P. Timoshenko, *J. Opt. Soc. Am.*, 1925, **11**, 233–255.

45 L. Moulet, N. Daro, C. Etrillard, J. F. Létard, A. Grosjean and P. Guionneau, *Magnetochemistry*, 2016, **2**, 10.

46 M. Piedrahita-Bello, K. Ridier, M. Mikolasek, G. Molnár, W. Nicolazzi, L. Salmon and A. Bousseksou, *Chem. Commun.*, 2019, **55**, 4769–4772.

47 G. Besendorfer and A. Roosen, *J. Am. Ceram. Soc.*, 2008, **91**, 2514–2520.

48 M. K. Panda, T. Runčevski, S. C. Sahoo, A. A. Belik, N. K. Nath, R. E. Dinnebier and P. Naumov, *Nat. Commun.*, 2014, **5**, 4811.

49 B. W. Rosen and Z. Hashin, *Int. J. Eng. Sci.*, 1970, **8**, 157–173.

50 R. M. McMeeking, *J. Am. Ceram. Soc.*, 1986, **69**, C-301.